



Article

Regulating Crystal Facets of MnO₂ for Enhancing Peroxymonosulfate Activation to Degrade Pollutants: Performance and Mechanism

Juncong Fu ^{1,†}, Peng Gao ^{2,†}, Lu Wang ¹, Yongqing Zhang ^{1,3,4,*}, Yuhui Deng ¹, Renfeng Huang ¹, Shuaifei Zhao ⁵ , Zebin Yu ⁶, Yuancheng Wei ⁷, Guangzhao Wang ⁸  and Shaoqi Zhou ⁹

¹ School of Environment and Energy, Guangdong Provincial Key Laboratory of Atmospheric Environment and Pollution Control, South China University of Technology, Guangzhou 510640, China; 201921045961@mail.scut.edu.cn (J.F.); 202020147168@mail.scut.edu.cn (L.W.); 201921045514@mail.scut.edu.cn (Y.D.); eshrf54321@mail.scut.edu.cn (R.H.)

² School of Chemistry and Molecular Bioscience, University of Wollongong, Wollongong, NSW 2500, Australia; pg177@uowmail.edu.au

³ The Key Lab of Pollution Control and Ecosystem Restoration in Industry Clusters, Ministry of Education, Guangzhou 510006, China

⁴ State Key Laboratory of Pulp and Paper, South China University of Technology, Guangzhou 510006, China

⁵ Institute for Frontier Materials, Deakin University, Geelong, VIC 3216, Australia; s.zhao@deakin.edu.au

⁶ School of Resources, Environment and Materials, Guangxi University, Nanning 530004, China; yuzebin@gxu.edu.cn

⁷ Preliminary Work Management Center for Government Investment Project of Shenzhen Longhua District, Shenzhen 518110, China; weiyuancheng1027@163.com

⁸ Key Laboratory of Extraordinary Bond Engineering and Advanced Materials Technology of Chongqing, School of Electronic Information Engineering, Yangtze Normal University, Chongqing 408100, China; wangyan6930@yznu.edu.cn

⁹ Guizhou Academy of Sciences, Shanxi Road 1, Guiyang 550001, China; fesqzhou@scut.edu.cn

* Correspondence: zhangyq@scut.edu.cn; Tel.: +86-13434389968; Fax: +86-20-39380508

† These authors contributed equally to this work.



Citation: Fu, J.; Gao, P.; Wang, L.; Zhang, Y.; Deng, Y.; Huang, R.; Zhao, S.; Yu, Z.; Wei, Y.; Wang, G.; et al.

Regulating Crystal Facets of MnO₂ for Enhancing Peroxymonosulfate Activation to Degrade Pollutants: Performance and Mechanism. *Catalysts* **2022**, *12*, 342. <https://doi.org/10.3390/catal12030342>

Academic Editor: Wenhui Wang

Received: 4 March 2022

Accepted: 15 March 2022

Published: 17 March 2022

Publisher's Note: MDPI stays neutral with regard to jurisdictional claims in published maps and institutional affiliations.



Copyright: © 2022 by the authors. Licensee MDPI, Basel, Switzerland. This article is an open access article distributed under the terms and conditions of the Creative Commons Attribution (CC BY) license (<https://creativecommons.org/licenses/by/4.0/>).

Abstract: On the catalyst surface, crystal facets with different surface atom arrangements and diverse physicochemical properties lead to distinct catalytic activity. Acquiring a highly reactive facet through surface regulation is an efficient strategy to promote the oxidative decomposition of wastewater organic pollutants via peroxymonosulfate (PMS) activation. However, the mechanism through which crystal facets affect PMS activation is still unclear. In this study, three facet-engineered α -MnO₂ with different exposed facets were prepared via a facile hydrothermal route. The prepared 310-MnO₂ exhibited superior PMS activation performance to 100-MnO₂ and 110-MnO₂. Moreover, the 310-MnO₂/PMS oxidative system was active over a wide pH range and highly resistant to interfering substances from wastewater. These advantages of the 310-MnO₂/PMS system make it highly promising for practical wastewater treatment. Based on quenching experiments, electron paramagnetic resonance (EPR) analysis, solvent exchange, and electrochemical measurements, mediated electron transfer was found to be the dominant nonradical pathway for *p*-chloroaniline (PCA) degradation. A sulfhydryl group (-SH) masking experiment showed that the highly exposed Mn atoms on the 310-MnO₂ surface were sites of PMS activation. In addition, density functional theory (DFT) calculations confirmed that the dominant {310} facet promoted adsorption/activation of PMS, which favored the formation of more metastable complexes on the α -MnO₂ surface. The reaction mechanism obtained here clarifies the relationship between PMS activation and crystal facets. This study provides significant insights into the rational design of high-performance catalysts for efficient water remediation.

Keywords: manganese dioxide; surface regulation; peroxymonosulfate activation; nonradical pathway; crystal facet dependence

1. Introduction

In recent years, the environmental and health problems caused by non-biodegradable persistent organic pollutants (POPs) discharged into the aquatic environment have sounded an alarm, especially due to their fatal toxicity [1,2]. A multitude of treatment technologies, such as adsorption [3], membrane separation [4], biodegradation [5], and advanced oxidation processes (AOPs) [1], has been developed to protect aquatic systems against these refractory pollutants. Among these treatment technologies, AOPs are the most effective against organic pollutant removal owing to the abundance of powerful reactive oxygen species (ROSs) they produce [6,7]. Currently, many AOPs, such as the traditional Fenton system ($\text{Fe}^{2+}/\text{H}_2\text{O}_2$) [8], photocatalysis [9], ozonation [10], electrochemical oxidation [11], and their combinations [12], are commonly used for POP removal. However, high energy input and potential secondary pollution limit their applications.

Persulfate activation, an emerging AOP-like pollutant control approach, is of great interest since it overcomes the shortcomings above. Persulfate activation not only removes pollutants by generating highly active radicals (such as $E(\bullet\text{OH}/\text{OH}^-) = 1.8\text{--}2.7\text{ V}$ and $E(\text{SO}_4^{\bullet-}/\text{SO}_4^{2-}) = 2.5\text{--}3.1\text{ V}$), but also oxidatively decomposes pollutants by nonradical pathways (such as singlet oxygen ($^1\text{O}_2$), surface-activated complex, and direct electron transfer) [13]. Solid persulfates, including peroxydisulfate (PDS) and peroxymonosulfate (PMS), are more stable and easier to store and transport than H_2O_2 and O_3 [14]. Given its asymmetric structure, PMS is more easily activated by various catalysts than PDS [15]. Moreover, aqueous organic pollutants can be effectively removed by activated PMS.

Since PMS has a relatively low reactivity toward POPs, effective PMS activation is a prerequisite for its environmental remediation application. Compared to traditional energy-based PMS activation methods (e.g., heat, UV, and ultrasonic), transition metal (Co, Ni, Ag, Cu, Ru, V) catalyst-based PMS activation is more cost-effective and uses a simpler reactor/system configuration [16]. Although cobalt-based materials are among the best options for activating PMS [17], the secondary pollution from the leaching of cobalt ions would lead to adverse effects on the environment. Therefore, it is imperative to develop environmentally friendly transition metal oxide catalysts. MnO_2 is a promising alternative PMS activation catalyst due to its low cost, multiple Mn valence states, abundance, and environmental friendliness [18]. By tuning MnO_2 's surface properties, such as crystal facets [19], crystalline phase [16], material dimension [20], and the number of defects [21], the catalytic performance of MnO_2 towards PMS can be effectively enhanced. Unfortunately, the mechanism of this enhancement is still ambiguous. Thus, to design more efficient catalysts for water remediation, it is crucial to understand the relationship between the PMS activation process and the surface properties.

As an inherent surface property, the crystal facet induces specific physical and chemical surface activity due to the differences in its atomic distribution and the distorted electronic structure of its surface [22]. The adsorption and activation of reaction molecules on the catalyst surface are the key steps during the persulfate-catalyzed process. In addition, the microstructure of the material surface significantly affects the persulfate activation pathway, leading to enhanced catalytic efficiency [23]. Previous work [24] demonstrated that CuO crystal facets played an important role in PS activation. Similarly, it was reported that the $\delta\text{-MnO}_2$ $\{-111\}$ facet exhibited superior persulfate activation performance compared to the $\{001\}$ facet [19]. Based on the cases above, we reason that MnO_2 with different exposed crystal facets affects PMS activation efficiency. However, how crystal facets affect PMS activation is still unknown. Understanding PMS activation on the MnO_2 surface with different exposed facets is of great significance in designing high-performance PMS activation catalysts for organic pollutant removal.

In this study, three highly active nano- MnO_2 catalysts with different exposed facets were synthesized via the facile hydrothermal route. Taking PCA as the model contaminant, the catalytic performance of $\alpha\text{-MnO}_2$ towards PMS was proven to be effectively enhanced by selectively exposing the high-index $\{310\}$ facet. The factors affecting PCA degradation were systematically investigated. The resistance of the system to interfering

substances from wastewater was also evaluated by introducing humic acid and inorganic anions. Cyclic experiments and manganese ion leaching experiments were carried out to test the stability and reusability of 310-MnO₂. Different pollutants were degraded in the 310-MnO₂/PMS oxidative system to explore its broad applicability. Based on an intermediate analysis, three pathways of PCA degradation in the 310-MnO₂/PMS system were proposed. Combining experimental studies and DFT calculations, the mechanism through which the crystal facets affected PMS activation was attributed to the different surface atom arrangements and enhanced adsorption of PMS molecules on the 310-MnO₂ surface. Unfortunately, there are few studies on the enhancement of persulfate activation by regulating crystal facets of manganese oxide, and how crystal facets affect PMS activation is still unclear. Unlike previous studies of persulfate activation by MnO₂, which were mainly focused on morphology, crystal phase, defect regulation, and manganese-based composites, this work focuses on regulating the crystal surface of MnO₂ to enhance PMS activation. The effect of crystal facets on PMS activation was comprehensively and deeply studied. This work provides atomic-scale insights into the relationship between PMS activation performance and crystal facets, as well as theoretical guidance for the rational design of high-performance PMS catalysts for practical wastewater treatment.

2. Results and Discussion

2.1. Characterization of Catalyst

Three α -MnO₂ with different exposed facets were prepared via the facile hydrothermal method. The phase structure of the prepared materials was identified by XRD (Figure 1a). All the samples were consistent with pure α -MnO₂ (PDF #44-0141), which has a well-defined 2 × 2 tunnel structure. However, the XRD peak intensities of the samples differed. For the 310-MnO₂, the diffraction peak corresponding to the {310} facet was sharper than for the {100} and {110} facets. Therefore, the {310} facet was the dominant exposed crystal facet of 310-MnO₂. This result is consistent with previous reports [25]. Similarly, the MnO₂ catalysts with exposed {110} (green line Figure 1a) and {100} (cyan line Figure 1a) facets were identified.

Electron paramagnetic resonance (EPR) spectroscopy was employed to analyze the differences in oxygen vacancy content among the three MnO₂ catalysts (Figure 1b). However, unlike typical EPR spectra of oxygen vacancy [21,23,26], no obvious oxygen vacancy signal was observed in this work, which means that the oxygen vacancy content was negligible.

To obtain the data from the BET surface area and pore properties, the N₂ adsorption/desorption isotherms of the three MnO₂ catalysts were measured (Figure S1). The relevant data are provided in Table S1. The results demonstrate that the 310-MnO₂ had the largest surface area (116.0 m²/g), followed by 110-MnO₂ (104.9 m²/g) and 100-MnO₂ (67.8 m²/g). However, the order of the surface area sizes on the three MnO₂ catalysts was inconsistent with the catalytic activity observed in the organic pollutant degradation experiments, indicating that the specific surface area was not the decisive factor in the catalytic activity.

The morphologies of the obtained MnO₂ samples with different exposed facets were determined by FE-SEM and HR-TEM analysis. The FE-SEM images (Figure 1c–h) showed that all the MnO₂ samples exhibited a nanowire morphology. The 110-MnO₂ nanowire had a diameter of 60–70 nm and a length of several micrometers, while the 310-MnO₂ and 100-MnO₂ were thinner, with diameters of 40–50 nm. The energy-dispersive spectrometer (EDS) results (Figure S2) demonstrated that the surface of the 310-MnO₂ had the highest Mn/O ratio (1.41), followed by 100-MnO₂ (0.75) and 110-MnO₂ (0.51). The order of the Mn/O ratio on different exposed crystal facets was consistent with the theoretical atomic arrangement analysis (Figure 2(a4–c4)).

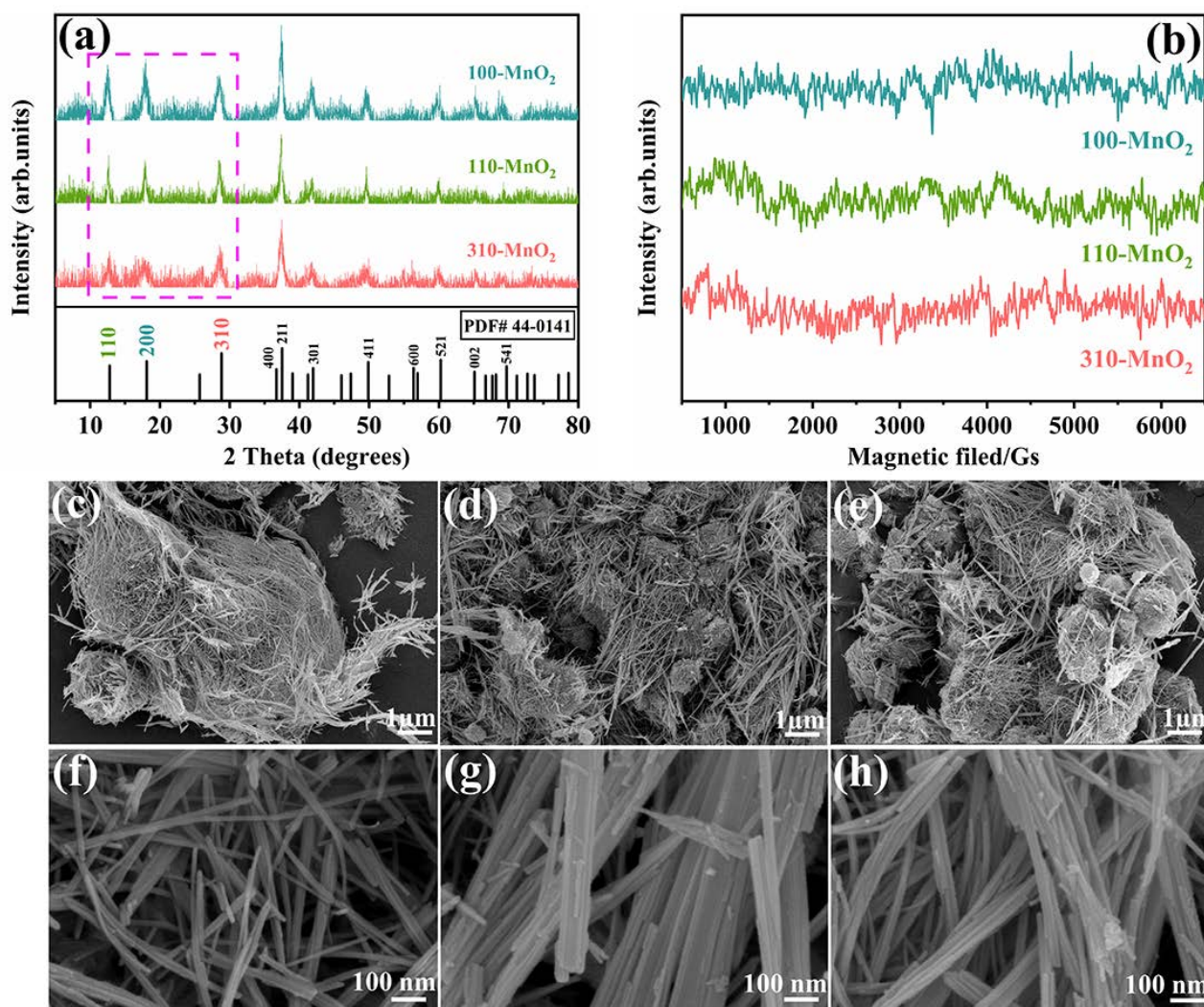


Figure 1. (a) XRD patterns of 100-MnO₂, 110-MnO₂, and 310-MnO₂; (b) solid EPR spectra of three MnO₂ catalysts; SEM images of (c,f) 100-MnO₂, (d,g) 110-MnO₂, and (e,h) 310-MnO₂.

HR-TEM further confirmed that the MnO₂ with different exposed crystal facets was synthesized successfully. The observed lattice distances of the {100}, {110}, and {310} facets were 0.49 nm, 0.69 nm, and 0.31 nm, respectively (Figure 2). These results agree with the calculated lattice distances based on XRD characterization, where the lattice distances for the facets were 4.90 Å {100}, 6.92 Å {110}, and 3.09 Å {310}, respectively. Since the α -MnO₂ grew along the (001) direction and had four exposed sides as the main exposed facet, it was easy to find that the 310-MnO₂ possessed four {310} facets exposed on the sides of the nanowires [25]. Similar phenomena were also found in the 100-MnO₂ and 110-MnO₂. Combined with the XRD results, the α -MnO₂ with different exposed crystal facets was successfully synthesized. By analyzing the atomic occupancy (Figure 2(a4–c4)) on the different facets, it was found that the exposed atoms on the {100} and {110} facets were mainly O, while Mn atoms were significantly enriched on the {310} facet. The MnO₂ with different crystal facets exhibited different PMS activation effects, which might have been due to different surface active sites, i.e., different Mn atom distributions on the surface [24]. Highly exposed surface Mn atoms might have facilitated electron transfer between the pollutants and the catalyst [27,28].

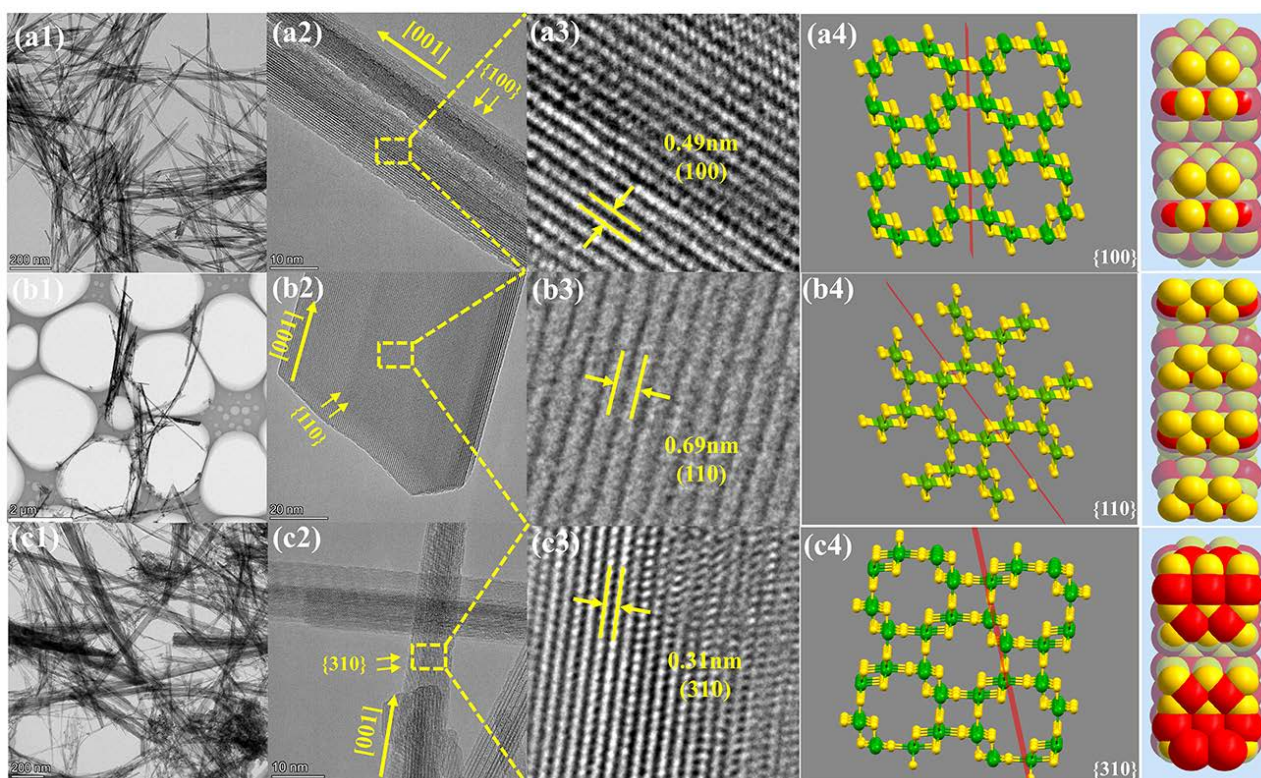


Figure 2. HRTEM images of (a1–a3) 100-MnO₂, (b1–b3) 110-MnO₂, and (c1–c3) 310-MnO₂; profile analysis and corresponding atom arrangement on the surface of (a4) 100-MnO₂, (b4) 110-MnO₂, and (c4) 310-MnO₂ in a 2 × 2 unit cell. Small (gold) spheres are oxygen and large (red and green) are manganese.

The surface chemical states and element composition of the obtained MnO₂ were investigated by XPS. The Mn 2p_{3/2} peak can be divided into three peaks, located at 642.9, 641.6, and 640.6 eV, corresponding to the binding energy of Mn⁴⁺, Mn³⁺, and Mn²⁺, respectively (Figure 3b) [29]. The ratio of the different types of Mn atom to the total Mn is summarized in Table S2. Meanwhile, the average oxidation state (AOS) of Mn (Figure 3c) was calculated by the equation $AOS = 8.956 - 1.126\Delta E$ (ΔE is the binding energy difference of Mn 3s) [30]. The AOS of different MnO₂ was essentially the same, which means a negligible difference in oxygen vacancy content. In other words, the enhancement of PMS activation on the MnO₂ with different facets was not related to the oxygen vacancy content. Moreover, the O 1s spectrum (Figure 3d) was divided into two peaks, located at 531.5 eV (surface-adsorbed oxygen (O_{ads}, such as O⁻, O²⁻ and -OH)) and 529.8 eV (lattice oxygen (O_{latt})) [22]. The relevant data are provided in Table S2. The chemical state of the Mn and the content of the oxygen species did not change significantly before or after the reaction, suggesting that the PMS activation process over the MnO₂ surface was a catalytic reaction.

2.2. PCA Degradation in the Facet-Engineered MnO₂/PMS System

2.2.1. PCA Degradation in Different α -MnO₂/PMS Systems

To investigate the PMS activation over MnO₂ with different facets, PCA was chosen as the target pollutant, and the PCA degradation experiments are displayed in Figure 4a. It was arduous to remove the PCA with α -MnO₂ alone, and only a 5% removal efficiency was achieved through adsorption. In the non-catalytic PMS system, the removal efficiency of the PCA over 5 min was about 10%, which indicated that the unactivated PMS had a limited ability to oxidize PCA. By contrast, 100% of the PCA was degraded within 5 min in the facet-engineered α -MnO₂/PMS systems, indicating that the facet-engineered α -MnO₂ catalyzed the production of more powerful oxidizing substances from the PMS

for PCA degradation. Interestingly, among the three facet-engineered α -MnO₂ catalysts, the 310-MnO₂ exhibited the best PMS activation performance, in which nearly 100% of the PCA was degraded in 3 min, while 67% and 84% of PCA were degraded in the 110-MnO₂/PMS and the 100-MnO₂/PMS systems, respectively. The reaction rate constant k of the 310-MnO₂/PMS system was three times that of the 110-MnO₂/PMS system (Figure 4b). Consequently, in subsequent optimization experiments, the 310-MnO₂ was chosen as the model catalyst for PMS activation.

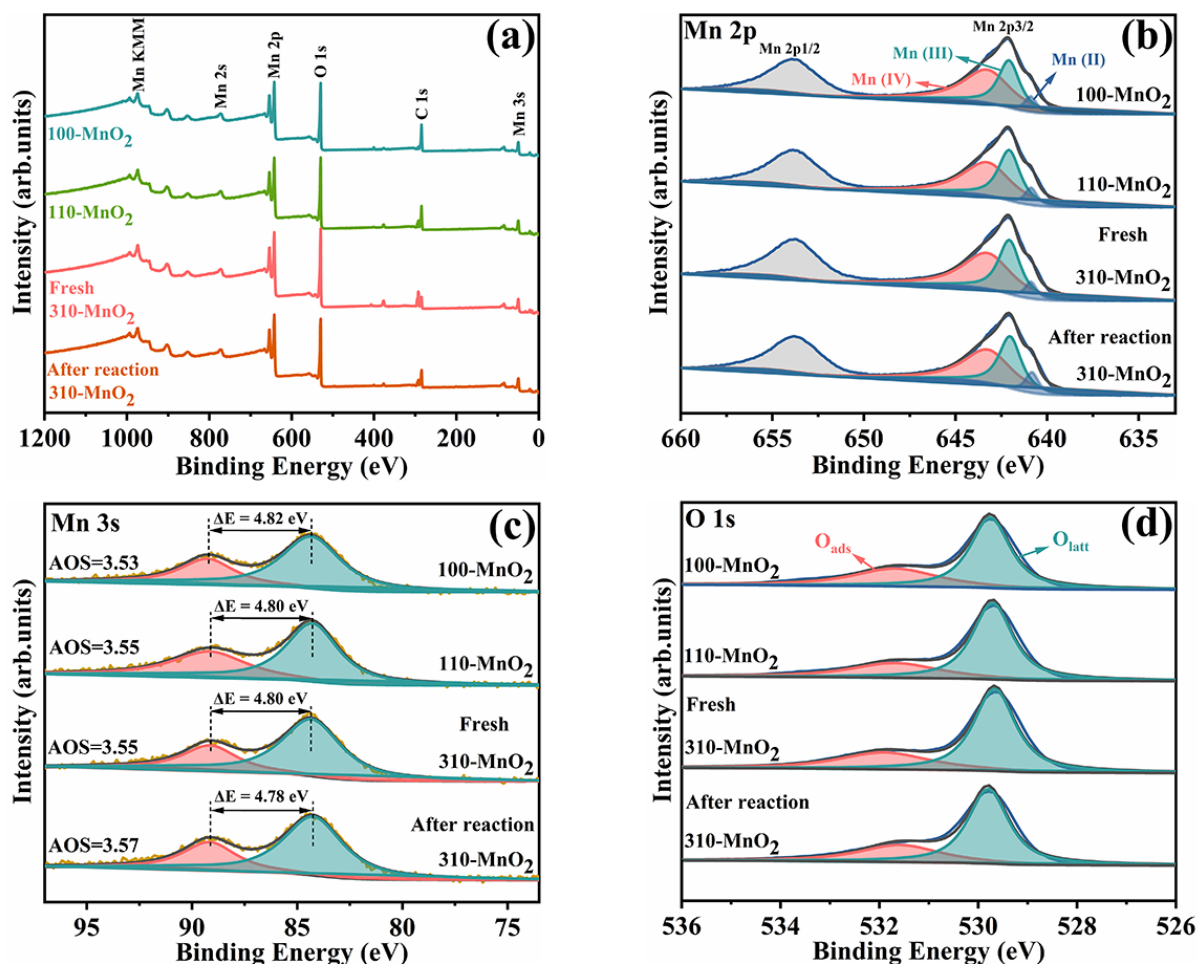


Figure 3. XPS spectra of α -MnO₂ with different exposed crystal facets: (a) survey spectra, (b) Mn 2p, (c) Mn 3s, and (d) O 1s.

2.2.2. Effect of PMS Concentration

The impact of the PMS concentration (0.5–3 mM) on the PCA degradation was evaluated (Figure 4c). Previous studies pointed out that in some heterogeneous PMS activation systems, excessive PMS had a negative impact on contaminant degradation [15,31,32]. However, in the 310-MnO₂/PMS system, increasing the PMS concentration increased the PCA degradation. With the PMS concentration increasing from 0.5 mM to 3 mM, the corresponding k value also increased, from 0.2003 min⁻¹ to 1.3916 min⁻¹ (Figure 4d). A similar phenomenon was observed in the edge-nitrogenated biochar/PDS system, in which pollutant degradation occurred through the electron transfer process (nonradical pathway) [33]. However, only a slight improvement was observed when the PMS exceeded 2 mM, suggesting insufficient active sites on the surface of 310-MnO₂ [34].

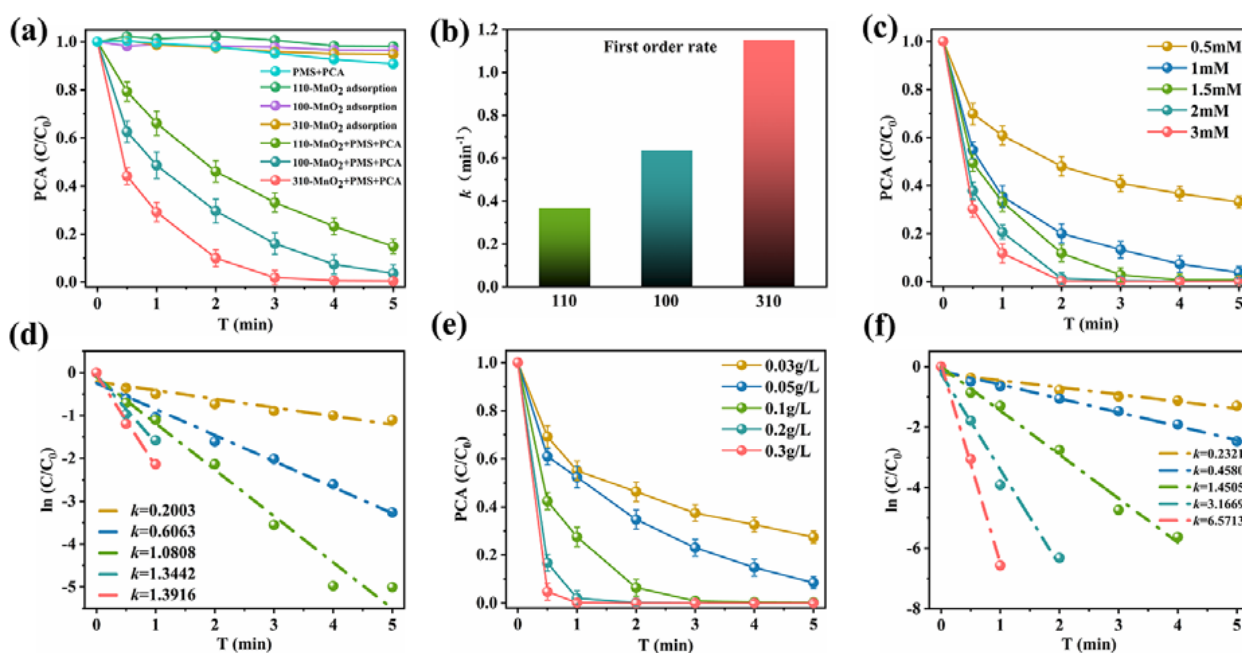


Figure 4. (a) Removal of PCA by different systems and (b) corresponding reaction rate constant k , reaction conditions: $(\text{PCA})_0 = 1.0 \text{ mM}$, $(\text{PMS})_0 = 1.5 \text{ mM}$, $(\text{MnO}_2)_0 = 0.1 \text{ g/L}$, without pH adjustment; (c) effect of PMS concentration in 310-MnO₂/PMS system and (d) corresponding linear fitting curve, reaction conditions: $(\text{PCA})_0 = 1.0 \text{ mM}$, $(\text{PMS})_0 = 0.5\text{--}3 \text{ mM}$, $(\text{MnO}_2)_0 = 0.1 \text{ g/L}$, without pH adjustment; (e) effect of MnO₂ dosage in the 310-MnO₂/PMS system and (f) corresponding linear fitting curve, reaction conditions: $(\text{PCA})_0 = 1.0 \text{ mM}$, $(\text{PMS})_0 = 1.5 \text{ mM}$, $(\text{MnO}_2)_0 = 0.03\text{--}0.3 \text{ g/L}$, without pH adjustment.

2.2.3. Effect of Catalyst Dosage

The catalyst dosage had a significant impact on the PCA degradation (Figure 4e). As the catalyst dosage increased from $0.03 \text{ g}\cdot\text{L}^{-1}$ to $0.3 \text{ g}\cdot\text{L}^{-1}$, the PCA degradation rate increased markedly from 0.2321 min^{-1} to 6.5713 min^{-1} (Figure 4f). In addition, the PCA degradation with different catalyst dosages fitted the pseudo-first-order kinetic model (Figure S3). The presence of more catalyst resulted in more active sites, facilitating PMS adsorption and activation on the MnO₂ surface [35]. Moreover, compared with the PMS concentration, the catalyst dosage played a more significant role in the PCA degradation. A similar phenomenon was also observed by Chen et al. [36], who found the sulfacetamide degradation rate was impacted more by the catalyst dosage than the PMS concentration.

2.2.4. Effect of Initial pH

The solution pH is a significant factor affecting the generation of ROSs in the chemical oxidation process [37]. Hence, the PCA removal efficiency under different initial pH conditions was systematically investigated. At an initial pH ranging from 3–9, the PCA was completely degraded within 5 min, indicating that the 310-MnO₂ was effective at activating the PMS over a wide initial pH range (Figure 5a). Moreover, the PMS was more easily activated at pH = 9 because the pK_a of PMS was 9.4 [18]; therefore, the 310-MnO₂/PMS system at pH = 9.0 exhibited a slightly higher PCA degradation rate than for pH = 3–7. The isoelectric point (pH_{pzc}) of 310-MnO₂ was 3.3 (Figure S4) and the pK_a of the PCA was 4.2 [38]. When the solution pH = 3, the catalyst surface was positively charged, which favored the adsorption of PMS anions on the catalyst surface, thereby achieving a marginally faster PCA degradation rate than at pH = 5–7.

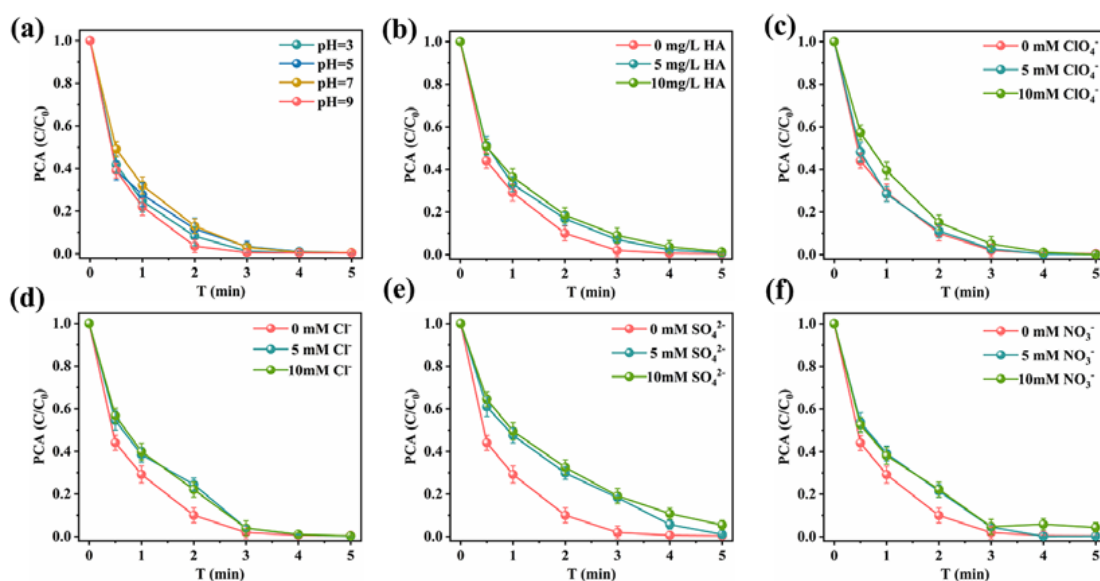


Figure 5. (a) Effect of initial pH, reaction conditions: $(\text{PCA})_0 = 1.0 \text{ mM}$, $(\text{PMS})_0 = 1.5 \text{ mM}$, $(\text{MnO}_2)_0 = 0.1 \text{ g/L}$, initial pH = 3–9; the influences of (b) humic acid, (c) ClO_4^- , (d) Cl^- , (e) SO_4^{2-} , and (f) NO_3^- , reaction conditions: $(\text{PCA})_0 = 1.0 \text{ mM}$, $(\text{PMS})_0 = 1.5 \text{ mM}$, $(\text{MnO}_2)_0 = 0.1 \text{ g/L}$, without pH adjustment.

2.3. Stability and Universal Adaptability

2.3.1. Universal Adaptability of 310-MnO₂

The natural organic matters (NOMs) and inorganic anions from actual water bodies tend to affect contaminant degradation during the PMS-based oxidation process by quenching radicals, generating other reactive species, or adsorbing on the catalyst surface [39–42]. For example, humic acid (HA) inhibits pollutant degradation by competing for reactive oxidizing substances [33]. Besides, another quintessential example is that Cl^- reacts with $\text{SO}_4^{\bullet-}$ and $\bullet\text{OH}$ to produce fewer reactive Cl^\bullet radicals, resulting in a significant inhibition of pollutant degradation [43]. Therefore, it is necessary to explore their influence on pollutant degradation in the 310-MnO₂/PMS system. In this work, the impact of HA and different co-existing anions (ClO_4^- , Cl^- , SO_4^{2-} , NO_3^-) on PCA degradation were investigated. As shown in Figure 5b, HA had little impact on PCA degradation. Furthermore, the presence of anions only slightly reduced the PCA degradation rate (Figure 5c–f), which is attributed to the negative impact of the increased ionic strength [44]. Due to fact that the solution pH ($\text{pH} \approx 3$) was lower than the isoelectric point of 310-MnO₂ ($\text{pH}_{\text{pzc}} = 3.3$), the catalyst surface was positively charged and could adsorb PMS anions. However, increased ionic strength reduces the zeta potential of catalyst particles in solution [43], which is unfavorable for the electrostatic attraction between the catalyst and the PMS. The above results suggested that the 310-MnO₂/PMS system was strongly resistant to interference.

Different pollutants, including PCA, Rhodamine B (RhB), phenol, tetracycline (TC), and imidacloprid (IMI), were degraded in the 310-MnO₂/PMS oxidative system to explore its broad applicability. As shown in Figure 6a, the 310-MnO₂/PMS system had an excellent removal effect on RhB and PCA: both were completely degraded within 5 min. Moreover, 100% of the phenol was removed in 15 min, while 80% of the TC was decomposed within 30 min. Interestingly, only 28% of the IMI was degraded in 30 min. Previous studies showed that radical systems degrade IMI effectively, while nonradical oxidation systems show low reactivity toward IMI [45]. Similarly, the selective removal of contaminants was also reported in other nonradical systems [34,46–48]. Thus, we speculated that the 310-MnO₂/PMS did not depend on free radicals.

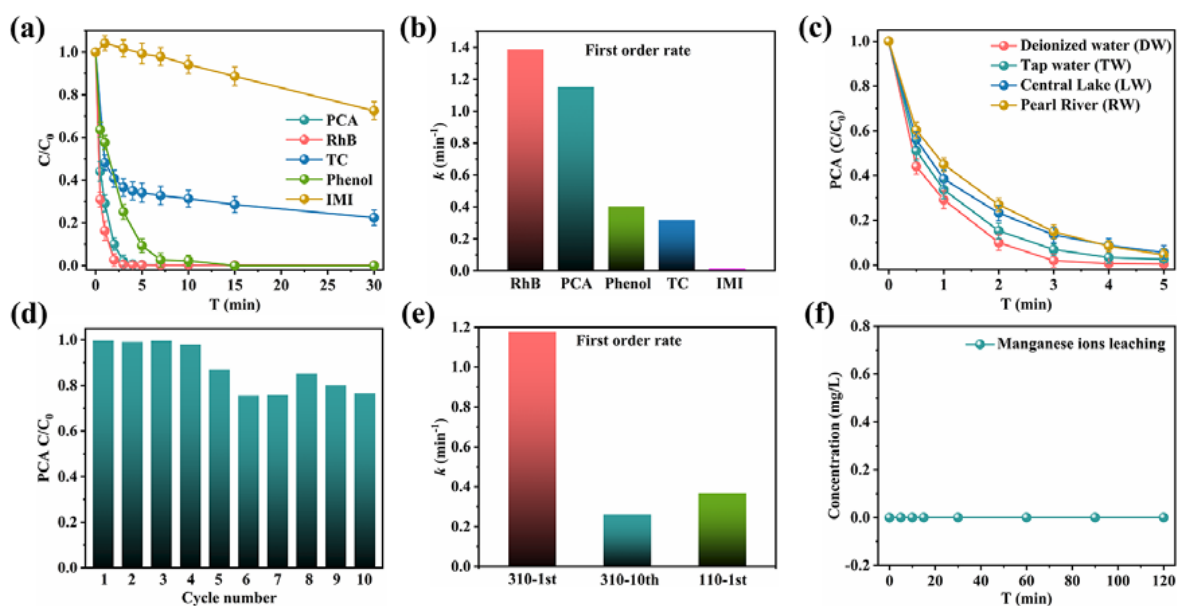


Figure 6. (a) Removal of various organic pollutants by 310-MnO₂/PMS system and (b) corresponding reaction rate constant *k*, reaction conditions: (PMS)₀ = 1.5 mM, (MnO₂)₀ = 0.1 g/L, (PCA)₀ = 1.0 mM, (RhB)₀ = 20 mg/L, (TC)₀ = 25 mg/L, (Phenol)₀ = 20 mg/L, (IMI)₀ = 10 mg/L, without pH adjustment; (c) degradation of PCA in actual water by 310-MnO₂/PMS system; (d) cycle tests of PCA degradation and (e) corresponding reaction rate constant *k*, reaction conditions: (PCA)₀ = 1.0 mM, (PMS)₀ = 1.5 mM, (MnO₂)₀ = 0.1 g/L, without pH adjustment; (f) the dissolution of manganese ions during the reaction, reaction conditions: (PCA)₀ = 1.0 mM, (PMS)₀ = 1.5 mM, (MnO₂)₀ = 0.1 g/L, without pH adjustment.

To further assess the potential of 310-MnO₂ in practical applications, PCA degradation experiments were carried out in deionized water (DW), tap water (TW), lake water (LW), and river water (RW) (Figure 6c). Compared with the rate in DW, the degradation rate of the PCA in actual water decreased slightly. However, after 5 min of reaction, the PCA removal rate still reached 97.5%, 94.4%, and 95.5% in TW, LW, and RW, respectively. The above results suggest that the 310-MnO₂/PMS system is highly promising for practical wastewater treatment.

2.3.2. Stability of 310-MnO₂

The stability of the catalytic materials is one of the core issues that needs to be considered before practical application. Materials with low stability increase the cost of operation and cause secondary pollution. Therefore, we carried out a cycle test (Figure 6d) to evaluate the stability of the 310-MnO₂. The results indicated that the 310-MnO₂ had high stability, with the PCA degradation efficiency remained at 80% after the 10th cycle. As the number of cycles increased, the PCA degradation rate constant (*k*) on the 310-MnO₂ slightly decreased, but the *k* value after the 10th cycle was still equivalent to that of the fresh 110-MnO₂ (Figure 6e). In addition, nearly no manganese ions were dissolved during the reaction process (Figure 6f). This result might have been caused by the material oxalate ions serving as a capping agent, both the stability and percentages of the {310} facet were improved [14,25]. Accordingly, the reason for the decrease in reaction rate might be related to the generated intermediate products adsorbing on the catalyst surface, thus inhibiting the exposure of the active sites [49]. Due to the 310-MnO₂'s outstanding stability and universal adaptability, it will have broad applications in actual wastewater treatment.

2.4. Mechanism of PMS Activation by 310-MnO₂

2.4.1. Quenching Experiments and PMS Decomposition Experiments

To unveil the PMS activation mechanism on the 310-MnO₂ catalyst, a series of quenching experiments were performed by adding different scavengers to the 310-MnO₂/PMS system. EtOH is commonly used as a scavenger for $\bullet\text{OH}$ ($k_{\bullet\text{OH}/\text{ethanol}} = 1.2 \times 10^9 - 2.8 \times 10^9 \text{ M}^{-1} \text{ S}^{-1}$) and $\text{SO}_4^{\bullet-}$ ($k_{\text{SO}_4^{\bullet-}/\text{ethanol}} = 1.6 \times 10^7 - 7.7 \times 10^7 \text{ M}^{-1} \text{ S}^{-1}$) due to its high reactivity [50]. TBA is an effective scavenger that distinguishes between $\text{SO}_4^{\bullet-}$ and $\bullet\text{OH}$, since its reaction rate with $\bullet\text{OH}$ ($k_{\bullet\text{OH}/\text{TBA}} = 3.8 \times 10^8 - 7.6 \times 10^8 \text{ M}^{-1} \text{ S}^{-1}$) is nearly 1000 times higher than with $\text{SO}_4^{\bullet-}$ ($k_{\text{SO}_4^{\bullet-}/\text{TBA}} = 4 \times 10^5 - 9.1 \times 10^5 \text{ M}^{-1} \text{ S}^{-1}$) [51,52]. The addition of 750 mM EtOH or 750 mM TBA showed a negligible impact on PCA oxidation (Figure 7a), suggesting that neither $\bullet\text{OH}$ nor $\text{SO}_4^{\bullet-}$ were the dominant active oxidizing species for PCA degradation. The *p*-BQ, with a high reaction rate constant with $\text{O}_2^{\bullet-}$ ($k_{\text{O}_2^{\bullet-}/p\text{-BQ}} = 0.9 - 1.0 \times 10^9 \text{ M}^{-1} \text{ S}^{-1}$), was selected to explore the possible role of $\text{O}_2^{\bullet-}$ in the reaction system [53]. However, the PCA degradation was not inhibited at all by the introduction of 1.5 mM or 15 mM *p*-BQ (Figure 7a), thus excluding the presence of $\text{O}_2^{\bullet-}$ in the 310-MnO₂/PMS system. The experimental results suggested that nonradical species rather than radicals played the dominant role in the PCA degradation. Based on previous reports, three major nonradical oxidation pathways were proposed, including singlet oxygen ($^1\text{O}_2$) oxidation, direct electron transfer, and surface-bound active species [13,54–57]. $^1\text{O}_2$ is a potential active oxidizing species that can be produced during PMS activation by transition metal oxide or carbon-based material [58–60]. To verify whether $^1\text{O}_2$ took part in the PCA degradation in 310-MnO₂/PMS system, FFA, a typical scavenger for $^1\text{O}_2$ ($k_{^1\text{O}_2/\text{FFA}} = 1.2 \times 10^8 \text{ M}^{-1} \text{ S}^{-1}$), was chosen [61]. The addition of 2.5 mM FFA only slightly inhibited the PCA degradation (Figure 7b). However, increasing the FFA to 75 mM inhibited nearly 40% of the PCA degradation.

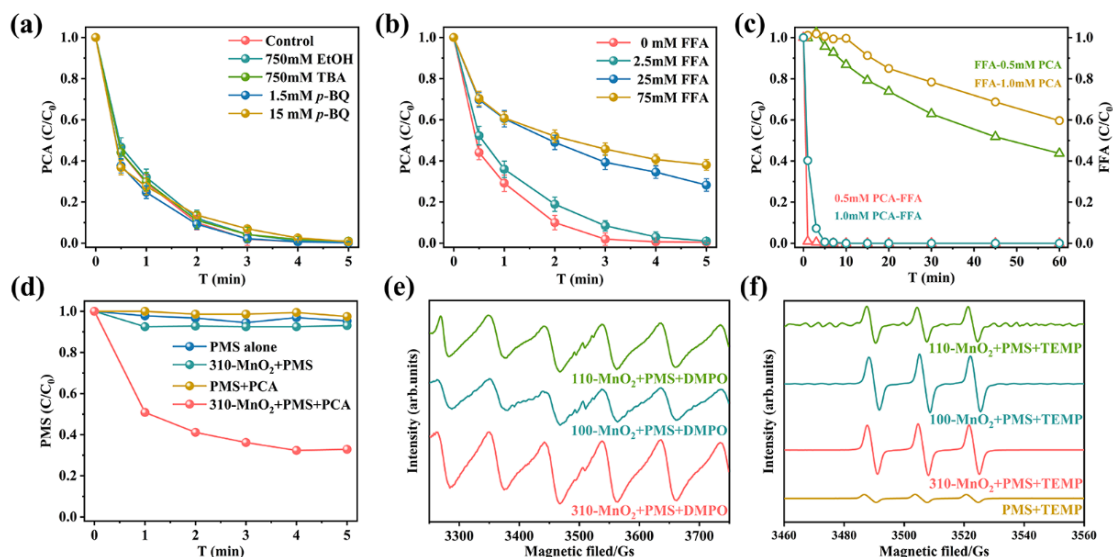


Figure 7. (a) PCA degradation in the presence of various free radical scavengers and (b) singlet oxygen scavenger, reaction conditions: $(\text{PCA})_0 = 1.0 \text{ mM}$, $(\text{PMS})_0 = 1.5 \text{ mM}$, $(\text{MnO}_2)_0 = 0.1 \text{ g/L}$, without pH adjustment; (c) FFA degradation by the 310-MnO₂/PMS system in the presence of PCA, reaction conditions: $(\text{PCA})_0 = 0.5\text{--}1.0 \text{ mM}$, $(\text{FFA})_0 = 0.1 \text{ mM}$, $(\text{PMS})_0 = 1.5 \text{ mM}$, $(\text{MnO}_2)_0 = 0.1 \text{ g/L}$, without pH adjustment; (d) decomposition of PMS in PMS alone, 310-MnO₂/PMS, PMS+PCA, 310-MnO₂/PMS/PCA systems, reaction conditions: $(\text{PCA})_0 = 1.0 \text{ mM}$, $(\text{PMS})_0 = 1.5 \text{ mM}$, $(\text{MnO}_2)_0 = 0.1 \text{ g/L}$, without pH adjustment; EPR signals of different PMS activation system with the existence of (e) DMPO and (f) TEMP, reaction conditions: $(\text{PMS})_0 = 1.5 \text{ mM}$, $(\text{MnO}_2)_0 = 0.1 \text{ g/L}$, $(\text{DMPO})_0 = 0.05 \text{ M}$, $(\text{TEMP})_0 = 0.1 \text{ M}$, without pH adjustment.

Further experiments were performed to investigate the removal of FFA with PCA present in the 310-MnO₂/PMS system. Considering that FFA has a high reaction rate constant with ¹O₂ ($k^1_{O_2/FFA} = 1.2 \times 10^8 \text{ M}^{-1} \text{ S}^{-1}$), if ¹O₂ is the dominant active oxidizing substance in the PCA degradation system, FFA is decomposed preferentially. However, it was found that the 310-MnO₂/PMS system preferentially decomposed the PCA oxidatively, and the FFA only began to degrade after the PCA was completely decomposed (Figure 7c). We also investigated the FFA degradation with different PCA concentrations (0.5 mM and 1 mM). Interestingly, the time when the FFA degradation began was delayed with increasing PCA concentration due to the preferential degradation of the increased PCA. These results indirectly indicate that ¹O₂ is not the main active oxidizing substance. The inhibition of PCA degradation by FFA is likely to have been due to the high concentration of FFA altering the surface properties of the catalyst, eventually resulting in the inhibition of pollutant adsorption and degradation [62].

The corresponding PMS consumption was also determined to reveal the possible PMS activation mechanism (Figure 7d). A slight decomposition of PMS was observed in the PMS-only, PMS/PCA, and 310-MnO₂/PMS systems. However, in the presence of PCA, notable PMS decomposition occurred in the 310-MnO₂/PMS system, suggesting that both 310-MnO₂ and PCA were necessary for efficient PMS decomposition. These results further excluded the existence of radicals.

2.4.2. EPR Detection and Solvent Exchange Experiment

To shed light on the PMS activation mechanism, EPR tests were conducted using TEMP to capture ¹O₂ and DMPO to capture short-lifetime radicals. The absence of classical radical adduct signals (Figure 7e) further confirmed that •OH, SO₄•⁻, and O₂•⁻ were not generated during the reaction. However, a clear six-line spectrum with a large span was observed in the EPR spectrum, which was attributed to Mn [63]. The ~3500 G signal was due to the direct oxidation of DMPO to DMPOX instead of a radical attack [32]. The PMS led to weak triplet signals (1:1:1) due to its small amount of self-decomposition (Figure 7f) [7]. As the catalysts were introduced into the PMS solution, a remarkable TEMPO triplet signal was obtained; this is usually employed as evidence for the existence of ¹O₂ [21,48]. However, solvent exchange (replacing H₂O with D₂O) (Figure 8a) did not accelerate the PCA degradation. As we know, the degradation rate of the oxidative system based on ¹O₂ should be faster in D₂O than in H₂O, since the lifetime of ¹O₂ in D₂O (20–32 μs) is significantly longer than in H₂O (2 μs) [64]. These contradictory results suggested that the TEMPO signal obtained in the 310-MnO₂/PMS system did not prove the formation of ¹O₂ [33]. Nardi et al. proposed that it may be misleading to detect ¹O₂ using the TEMPO/EPR method, since the excited intermediate also can extract one electron from TEMP to form TEMP⁺, which combines with the dissolved oxygen to generate TEMPO [65]. A similar phenomenon was also observed in the edge-nitrogenated biochar/PDS system, in which pollutant degradation occurred through the electron transfer process [33]. In addition, a significant increase in dissolved oxygen (DO) concentration was observed (Figure 8b) in a typical singlet oxygen system (*p*-BQ/PMS), which is consistent with the research of Zhou et al. [66]. However, no significant DO increase occurred in the 310-MnO₂/PMS system. Therefore, ¹O₂ did not contribute to PCA degradation in the 310-MnO₂/PMS system.

2.4.3. Electrochemical Analysis and Sulfhydryl Modification Experiments

According to the above results, other nonradical pathways, instead of ¹O₂, may be involved in the 310-MnO₂/PMS/PCA system. The electron transfer pathway was confirmed in some single-atom catalysts, transition metal oxide catalysts, and carbon-based materials [18,32,33,49]. To further identify the oxidative mechanism in our system, cyclic voltammetry (CV) experiments were carried out. The current density of the 310-MnO₂ changed slightly after adding PMS (Figure 8c). The slight charge rearrangement between the catalyst and PMS to form a metastable complex might have been responsible for this [67]. However, an apparent increase in the current density appeared once the PCA was

introduced, indicating that a current flow formed from PCA to the metastable complex [32]. The interaction between the 310-MnO₂ and PMS was confirmed by ATR-FTIR. A red-shift of about 8 cm⁻¹ was observed at the wavelength of 1095 cm⁻¹ (S-O stretching) when the 310-MnO₂ was added into the PMS solution (Figure S5a), suggesting the formation of complexes on the 310-MnO₂ surface [16,18]. Moreover, both a strong reduction and oxidation peaks were observed in the CV curves, suggesting the reversibility of the process, which is essential for continuous PMS activation.

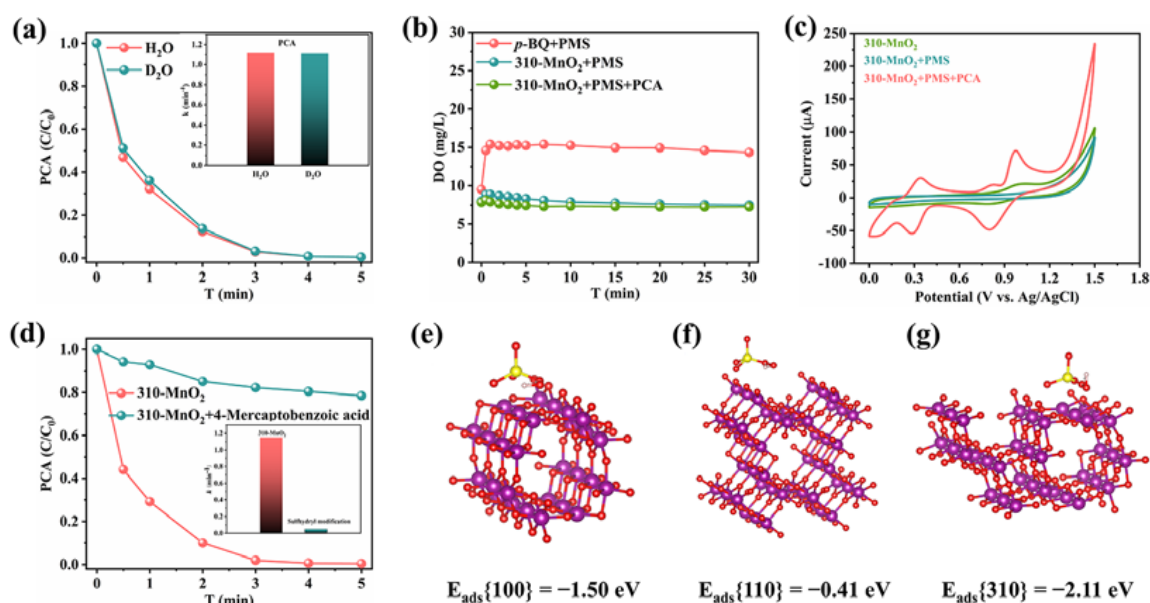


Figure 8. (a) Effect of reaction solvents (H₂O and D₂O) and corresponding reaction rate constant *k*, reaction conditions: (PCA)₀ = 1.0 mM, (PMS)₀ = 1.5 mM, (MnO₂)₀ = 0.1 g/L, without pH adjustment; (b) dissolved oxygen changes in different systems, (PCA)₀ = 1.0 mM, (PMS)₀ = 1.5 mM, (MnO₂)₀ = 0.1 g/L, (p-BQ)₀ = 20 μM, without pH adjustment; (c) CV curves obtained under different conditions; (d) PCA removal in 310-MnO₂/PMS system after surface manganese atom block and corresponding reaction rate constant *k*, reaction conditions: (PCA)₀ = 1.0 mM, (PMS)₀ = 1.5 mM, (MnO₂)₀ = 0.1 g/L, without pH adjustment; adsorption energy of PMS over α-MnO₂ with different exposed crystal facets: (e) 100-MnO₂, (f) 110-MnO₂, and (g) 310-MnO₂.

As mentioned above, the exposed atoms on the {100} and {110} facet were mainly O, while many Mn atoms were enriched in the surface of the {310} facet. To determine whether the surface Mn atoms were the sites of PMS activation, the sulfhydrylization reagent 4-mercaptobenzoic acid was employed to block surface Mn atoms through complexation between the Mn and the sulfhydryl group [24]. After modification with 4-mercaptobenzoic acid, a characteristic peak of the thiophenol S-H bond appeared at 2561 cm⁻¹ in the 310-MnO₂ FTIR (Figure S5b), indicating that the modification was successful. In addition, PCA degradation was almost completely inhibited in the 310-MnO₂/PMS system after surface modification with the -SH group (Figure 8d), confirming that Mn atoms on the catalyst surface were sites of PMS activation. Thus, in the 310-MnO₂/PMS/PCA system, PMS was adsorbed on the surface Mn sites, forming a metastable complex. Next, the PCA was adsorbed on the metastable complex surface through a “donor-acceptor complex” mechanism. There, the 310-MnO₂ served as a bridge for electron transfer between the PCA and the PMS.

2.4.4. DFT Calculations

Crystal facet engineering can modify surface atomic distribution and decrease adsorption energy [19]. To further explore why different crystal facets of α-MnO₂ produce distinct catalytic performances, the adsorption energies of the PMS molecule on the α-

MnO₂ surface were calculated using density functional theory (DFT). The DFT calculation method is provided in Text S1. The adsorption energies (E_{ads}) of the PMS molecules over the α -MnO₂ with {100}, {110}, and {310} facets were -1.50 eV, -0.41 eV, and -2.11 eV, respectively (Figure 8e–g). Due to the relatively negative adsorption energy and the highly exposed surface Mn atoms of the {310} facet, the PMS molecules were easily adsorbed on the {310} facet to form more metastable complexes, thereby promoting PMS activation and pollutant degradation.

2.5. Removal of TOC and Proposed Pathway of PCA Degradation

To investigate the mineralization of PCA degradation, the degradation of the total organic carbon (TOC) in the PCA by the 310-MnO₂/PMS system was tested (Figure S6). In 120 min, 67.6% of the TOC was removed, indicating the incomplete mineralization of the PCA and the generation of intermediates.

Interestingly, the solution changed from colorless to wine-red during the reaction, indicating the presence of chromophore in the intermediate products, possibly due to the formation of $-\text{N}=\text{N}-$. GC-MS was further used to understand the degradation pathway of the PCA in the 310-MnO₂/PMS system. Possible intermediate products are provided in Figure S7, and three pathways of PCA degradation are proposed (Figure 9). In the first pathway (I), one molecule of PCA loses the Cl atom, the other molecule loses the amino group ($-\text{NH}_2$), and they further dimerize to form *N*-(4-chloro-phenyl)-benzene-1,4-diamine (a). Next, hydroquinone (b) was produced from the oxidation of (a) [68]. In the second pathway (II), the PCA molecule was first dechlorinated to produce aniline (c) and then reacted to form azobenzene (d) [34]. In the third pathway (III), two PCA molecules dimerized to generate 4,4'-dichloroazobenzene (e). Although further intermediates were not detected, 4-chloro-phenyl-diazen (f) was reported as an oxidation by-product of (e) [68]. Finally, the PCA and its intermediates were mineralized into H₂O and CO₂.

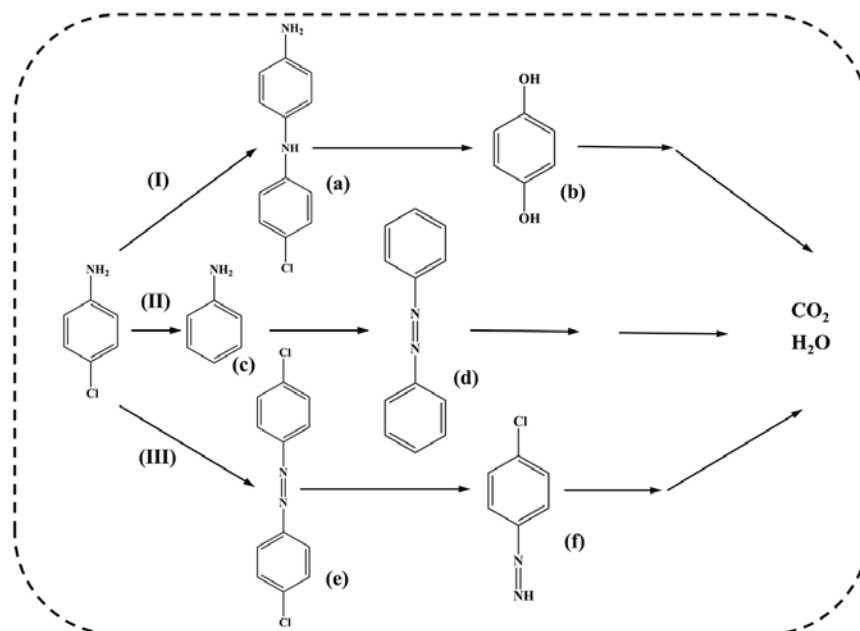


Figure 9. Three proposed pathways of PCA degradation in the 310-MnO₂/PMS system.

3. Materials and Methods

3.1. Chemicals

All chemicals used in the experiments were analytical (AR)- or HPLC-grade. Detailed information is shown in the Supporting Information (Text S2).

3.2. Preparation of α -MnO₂ with Different Facets

Synthesis of 310-MnO₂: In a typical procedure, KMnO₄ (3.161 g, 20 mmol) and (NH₄)₂C₂O₄·H₂O (1.421 g, 10 mmol) were mixed in deionized (DI) water (70 mL) under magnetic stirring for 30 min. The solution was then transferred to a Teflon-lined stainless-steel autoclave and kept at 180 °C for 24 h. After the reaction was finished, the obtained precipitates were further washed several times with DI water and ethanol, and then dried at 105 °C for 24 h.

Synthesis of 110-MnO₂: 110-MnO₂ was carried out by the same route as for 310-MnO₂, but (NH₄)₂C₂O₄ was replaced by (NH₄)₂SO₄.

Synthesis of 100-MnO₂: In a typical procedure, MnSO₄·H₂O (1.352 g, 8 mmol), (NH₄)₂S₂O₈ (1.826 g, 8 mmol), (NH₄)₂SO₄ (1.982 g, 15 mmol), and KNO₃ (0.809 g, 8 mmol) were mixed in DI water (40 mL) under magnetic stirring for 30 min. Next, the mixture was transferred to a Teflon-lined stainless-steel autoclave and kept at 120 °C for 20 h. The obtained precipitates were further washed several times with DI water and ethanol, and then dried at 105 °C for 24 h.

3.3. Experimental Procedures

All solutions were prepared with DI water. Batch experiments were carried out in 150-millilitre conical flasks containing 100 mL reaction solution with magnetic stirring (650 rpm). To completely disperse the catalyst into water solution, 10 mg catalyst was added to 90 mL of DI water and sonicated for 5 min before the catalytic reaction. Next, 10 mL of 10 mM PCA and 46 mg of PMS were added in sequence. At the given time intervals, 0.5 mL of the mixture was removed and filtered (0.45 μ m), and the reaction was terminated by adding Na₂S₂O₃ (1 M, 0.5 mL).

To assess the effect of solution pH on PMS activation, the initial solution pH of the reaction system was adjusted to the desired value with NaOH (0.1 mol/L) or H₂SO₄ (0.1 mol/L). Experiments with varying PMS concentrations, amounts of catalyst and anion species were conducted to investigate the influence of these parameters. Quenching experiments were carried out utilizing EtOH, TBA, *p*-BQ, and FFA as quenchers.

3.4. Analytical Techniques

A scanning electron microscope (SEM, SU8010, Hitachi Limited, Tokyo, Japan) was used to observe the surface morphology of the materials. A transmission electron microscope (TEM, Talos F200X, FEI, Hillsboro, OR, USA) was used to observe the morphology and exposed crystal facet of the materials. The phase structure of the catalysts was characterized by an X-ray diffractometer (XRD, D8 Advance, Bruker, Karlsruhe, Germany). X-ray photoelectron spectrometry (XPS, PHI X-tool, ULVAC-PHI, Chigasaki, Kanagawa, Japan) was used to investigate the chemical valence and composition of the catalysts. The surface interaction between the 310-MnO₂ and PMS was confirmed by Fourier-transform infrared spectroscopy (ATR-FTIR, Thermo Scientific iD5 and Thermo Scientific Nicolet iS5, Shanghai Linglu Instrument Equipment Co., Ltd., Shanghai, China).

Pollutant concentrations were determined by high-performance liquid chromatography (HPLC) equipped with a reversed-phase C18 column (250 mm \times 4.6 mm). Analytical details for the organic compounds are provided in the Supporting Information (Table S3). The PMS concentration was determined by the iodide ion color spectrometry [69]. The manganese ion leaching during the reaction process was detected by ICP-OES (Optima 8300, PerkinElmer, Waltham, MA, USA). The dissolved oxygen concentration in the reaction solution was determined by a portable dissolved oxygen analyzer (ST300D, Ohaus, Changzhou, China). Total organic carbon (TOC) was measured by an Elementar vario TOC (Elementar Analysensysteme GmbH, Hanau, Germany). Radicals in solution were analyzed by electron paramagnetic resonance (Bruker A300, Bruker, Karlsruhe, Germany). The parameters were set as follows: microwave frequency 9.8752 GHz, sweep width 100 G, center field 2504.12 G, modulation amplitude 1 G, time constant 327.68 ms, and sweep time 40 s.

4. Conclusions

In summary, three α -MnO₂ with different dominant exposed crystal facets were successfully prepared via the facile hydrothermal route. The prepared 310-MnO₂ exhibited excellent PMS activation performance and extremely high stability. In addition, the 310-MnO₂/PMS system could degrade a wide range of pollutants and remove the target pollutants effectively in an actual water body. More importantly, the 310-MnO₂/PMS oxidative system exhibited a wide pH adaptation range and showed good selectivity in the presence of natural organic matter and inorganic anions. The quenching experiments, EPR analysis, solvent exchange, and CV curves demonstrated that mediated electron transfer was the dominant mechanism in the PCA degradation. During the reaction, the electron was transferred from the adsorbed PCA (as an electron donor) to the adsorbed PMS (as an electron acceptor) on the catalyst's surface with the 310-MnO₂ acting as an electron transporter. The Mn atoms on the catalyst surface were confirmed to be sites of PMS activation by modifying MnO₂ with -SH group. The DFT calculations verified that PMS molecules can be strongly adsorbed on the {310} facet with low adsorption energy, thereby promoting PMS activation and pollutant degradation. In this study, we demonstrated that for transition metal oxides, the dominant exposed facets significantly affect PMS activation. The reaction mechanism we discovered provides guidance for the design of novel and efficient wastewater treatment catalysts.

Supplementary Materials: The following supporting information can be downloaded at: <https://www.mdpi.com/article/10.3390/catal12030342/s1>, Text S1: DFT Calculation Method; Text S2: Reagents used in the experiment; Text S3: Experimental sample preparation; Table S1: Properties of the three MnO₂ catalysts; Table S2: Chemical and surface compositions of facet engineered MnO₂ before and after the reaction; Table S3: Analytical details for organic compounds by HPLC; Figure S1: The N₂ adsorption/desorption isotherms of the three MnO₂ catalysts; Figure S2: EDS-mapping images of (a) 100-MnO₂, (b) 110-MnO₂, and (c) 310-MnO₂; Figure S3: (a) Effect of MnO₂ dosage in 310-MnO₂/PMS system and (b) correlation of the rate constants to the MnO₂ dosage; Figure S4: The zeta potential curves of the 310-MnO₂; Figure S5: (a) ATR-FTIR spectra demonstrating the PMS complexation on the catalyst surface and (b) ATR-FTIR spectra of 310-MnO₂ solid before and after modifying with -SH group; Figure S6: TOC removal of PCA degradation with 310-MnO₂/PMS system; Figure S7: Mass spectra and proposed structure of possible intermediate products.

Author Contributions: Conceptualization, J.F.; Funding acquisition, Y.Z.; Investigation, J.F.; Methodology, J.F., P.G., L.W. and G.W.; Resources, Y.W.; Software, J.F., P.G., L.W. and G.W.; Supervision, Y.Z., Z.Y. and S.Z. (Shaoqi Zhou); Validation, Y.Z.; Writing—original draft, J.F.; Writing—review & editing, Y.Z., Y.D., R.H., S.Z. (Shuaifei Zhao), Z.Y. and S.Z. (Shaoqi Zhao). All authors have read and agreed to the published version of the manuscript.

Funding: This work was financially supported by the National Key Research and Development Program of China (2016YFC0400708), the National Natural Science Foundation of China (51572089), the Natural Science Foundation of Guangdong Province, China (2019A1515011761) and the Foundation of Science and Technology Planning Project of Guangzhou, China (201804010398).

Data Availability Statement: Data is contained within the article or Supplementary Materials.

Conflicts of Interest: The authors declare that they have no known competing financial interests or personal relationships that could have appeared to influence the work reported in this paper.

References

1. Wang, J.; Wang, S. Activation of persulfate (PS) and peroxymonosulfate (PMS) and application for the degradation of emerging contaminants. *Chem. Eng. J.* **2018**, *334*, 1502–1517. [[CrossRef](#)]
2. Wang, J.; Wang, S. Removal of pharmaceuticals and personal care products (PPCPs) from wastewater: A review. *J. Environ. Manag.* **2016**, *182*, 620–640. [[CrossRef](#)] [[PubMed](#)]
3. Dąbrowski, A.; Podkościelny, P.; Hubicki, Z.; Barczak, M. Adsorption of phenolic compounds by activated carbon—A critical review. *Chemosphere* **2005**, *58*, 1049–1070. [[CrossRef](#)] [[PubMed](#)]
4. Kim, S.; Chu, K.H.; Al-Hamadani, Y.A.; Park, C.M.; Jang, M.; Kim, D.-H.; Yu, M.; Heo, J.; Yoon, Y. Removal of contaminants of emerging concern by membranes in water and wastewater: A review. *Chem. Eng. J.* **2018**, *335*, 896–914. [[CrossRef](#)]

5. Haritash, A.; Kaushik, C. Biodegradation aspects of Polycyclic Aromatic Hydrocarbons (PAHs): A review. *J. Hazard. Mater.* **2009**, *169*, 1–15. [[CrossRef](#)] [[PubMed](#)]
6. Wu, S.; Liu, H.; Yang, C.; Li, X.; Lin, Y.; Yin, K.; Sun, J.; Teng, Q.; Du, C.; Zhong, Y. High-performance porous carbon catalysts doped by iron and nitrogen for degradation of bisphenol F via peroxymonosulfate activation. *Chem. Eng. J.* **2019**, *392*, 123683. [[CrossRef](#)]
7. Li, H.; Tian, J.; Zhu, Z.; Cui, F.; Zhu, Y.-A.; Duan, X.; Wang, S. Magnetic nitrogen-doped nanocarbons for enhanced metal-free catalytic oxidation: Integrated experimental and theoretical investigations for mechanism and application. *Chem. Eng. J.* **2018**, *354*, 507–516. [[CrossRef](#)]
8. Pignatello, J.J.; Oliveros, E.; Mackay, A. Advanced Oxidation Processes for Organic Contaminant Destruction Based on the Fenton Reaction and Related Chemistry. *Crit. Rev. Environ. Sci. Technol.* **2006**, *36*, 1–84. [[CrossRef](#)]
9. Xu, X.; Wang, J.; Chen, T.; Yang, N.; Wang, S.; Ding, X.; Chen, H. Deep insight into ROS mediated direct and hydroxylated dichlorination process for efficient photocatalytic sodium pentachlorophenate mineralization. *Appl. Catal. B Environ.* **2021**, *296*, 120352. [[CrossRef](#)]
10. Tay, K.S.; Madehi, N. Ozonation of ofloxacin in water: By-products, degradation pathway and ecotoxicity assessment. *Sci. Total Environ.* **2015**, *520*, 23–31. [[CrossRef](#)]
11. Martínez-Huitle, C.A.; Brillas, E. Decontamination of wastewaters containing synthetic organic dyes by electrochemical methods: A general review. *Appl. Catal. B Environ.* **2009**, *87*, 105–145. [[CrossRef](#)]
12. Aziz, K.H.H. Application of different advanced oxidation processes for the removal of chloroacetic acids using a planar falling film reactor. *Chemosphere* **2019**, *228*, 377–383. [[CrossRef](#)] [[PubMed](#)]
13. Zhou, X.; Zhao, Q.; Wang, J.; Chen, Z.; Chen, Z. Nonradical oxidation processes in PMS-based heterogeneous catalytic system: Generation, identification, oxidation characteristics, challenges response and application prospects. *Chem. Eng. J.* **2020**, *410*, 128312. [[CrossRef](#)]
14. Wu, L.; Li, B.; Li, Y.; Fan, X.; Zhang, F.; Zhang, G.; Xia, Q.; Peng, W. Preferential Growth of the Cobalt (200) Facet in Co@N-C for Enhanced Performance in a Fenton-like Reaction. *ACS Catal.* **2021**, *11*, 5532–5543. [[CrossRef](#)]
15. He, D.; Li, Y.; Lyu, C.; Song, L.; Feng, W.; Zhang, S. New insights into MnOOH/peroxymonosulfate system for catalytic oxidation of 2,4-dichlorophenol: Morphology dependence and mechanisms. *Chemosphere* **2020**, *255*, 126961. [[CrossRef](#)]
16. Huang, J.; Dai, Y.; Singewald, K.; Liu, C.-C.; Saxena, S.; Zhang, H. Effects of MnO₂ of different structures on activation of peroxymonosulfate for bisphenol A degradation under acidic conditions. *Chem. Eng. J.* **2019**, *370*, 906–915. [[CrossRef](#)]
17. Hu, P.; Long, M. Cobalt-catalyzed sulfate radical-based advanced oxidation: A review on heterogeneous catalysts and applications. *Appl. Catal. B: Environ.* **2016**, *181*, 103–117. [[CrossRef](#)]
18. Huang, K.Z.; Zhang, H.J. Direct Electron-Transfer-Based Peroxymonosulfate Activation by Iron-Doped Manganese Oxide (δ -MnO₂) and the Development of Galvanic Oxidation Processes (GOPs). *Environ. Sci. Technol.* **2019**, *53*, 12610–12620. [[CrossRef](#)]
19. Wang, Z.; Jia, H.; Liu, Z.; Peng, Z.; Dai, Y.; Zhang, C.; Guo, X.; Wang, T.; Zhu, L. Greatly enhanced oxidative activity of δ -MnO₂ to degrade organic pollutants driven by dominantly exposed {–111} facets. *J. Hazard. Mater.* **2021**, *413*, 125285. [[CrossRef](#)]
20. Dong, Q.; Wang, J.; Duan, X.; Tan, X.; Liu, S.; Wang, S. Self-assembly of 3D MnO₂/N-doped graphene hybrid aerogel for catalytic degradation of water pollutants: Structure-dependent activity. *Chem. Eng. J.* **2019**, *369*, 1049–1058. [[CrossRef](#)]
21. Yu, J.; Zeng, T.; Wang, H.; Zhang, H.; Sun, Y.; Chen, L.; Song, S.; Li, L.; Shi, H. Oxygen-defective MnO_{2-x} rattle-type microspheres mediated singlet oxygen oxidation of organics by peroxymonosulfate activation. *Chem. Eng. J.* **2020**, *394*, 124458. [[CrossRef](#)]
22. He, C.; Wang, Y.; Li, Z.; Huang, Y.; Liao, Y.; Xia, D.; Lee, S.-C. Facet Engineered α -MnO₂ for Efficient Catalytic Ozonation of Odor CH₃SH: Oxygen Vacancy-Induced Active Centers and Catalytic Mechanism. *Environ. Sci. Technol.* **2020**, *54*, 12771–12783. [[CrossRef](#)] [[PubMed](#)]
23. Huang, R.; Zhu, Y.; Curnan, M.T.; Zhang, Y.; Han, J.W.; Chen, Y.; Huang, S.; Lin, Z. Tuning reaction pathways of peroxymonosulfate-based advanced oxidation process via defect engineering. *Cell Rep. Phys. Sci.* **2021**, *2*, 100550. [[CrossRef](#)]
24. Du, X.; Zhang, Y.; Si, F.; Yao, C.; Du, M.; Hussain, I.; Kim, H.; Huang, S.; Lin, Z.; Hayat, W. Persulfate non-radical activation by nano-CuO for efficient removal of chlorinated organic compounds: Reduced graphene oxide-assisted and CuO (0 0 1) facet-dependent. *Chem. Eng. J.* **2018**, *356*, 178–189. [[CrossRef](#)]
25. Rong, S.; Zhang, P.; Liu, F.; Yang, Y. Engineering Crystal Facet of α -MnO₂ Nanowire for Highly Efficient Catalytic Oxidation of Carcinogenic Airborne Formaldehyde. *ACS Catal.* **2018**, *8*, 3435–3446. [[CrossRef](#)]
26. Liu, L.; Liu, Q.; Wang, Y.; Huang, J.; Wang, W.; Duan, L.; Yang, X.; Yu, X.; Han, X.; Liu, N. Nonradical activation of peroxydisulfate promoted by oxygen vacancy-laden NiO for catalytic phenol oxidative polymerization. *Appl. Catal. B Environ.* **2019**, *254*, 166–173. [[CrossRef](#)]
27. Xie, X.; Li, Y.; Liu, Z.-Q.; Haruta, M.; Shen, W. Low-temperature oxidation of CO catalysed by Co₃O₄ nanorods. *Nature* **2009**, *458*, 746–749. [[CrossRef](#)]
28. Tian, N.; Zhou, Z.-Y.; Sun, S.-G.; Ding, Y.; Wang, Z.L. Synthesis of Tetrahedral Platinum Nanocrystals with High-Index Facets and High Electro-Oxidation Activity. *Science* **2007**, *316*, 732–735. [[CrossRef](#)]
29. Wang, F.; Dai, H.; Deng, J.; Bai, G.; Ji, K.; Liu, Y. Manganese Oxides with Rod-, Wire-, Tube-, and Flower-Like Morphologies: Highly Effective Catalysts for the Removal of Toluene. *Environ. Sci. Technol.* **2012**, *46*, 4034–4041. [[CrossRef](#)]
30. Yang, Y.; Huang, J.; Wang, S.; Deng, S.; Wang, B.; Yu, G. Catalytic removal of gaseous unintentional POPs on manganese oxide octahedral molecular sieves. *Appl. Catal. B Environ.* **2013**, *142–143*, 568–578. [[CrossRef](#)]

31. Fan, J.; Zhao, Z.; Ding, Z.; Liu, J. Synthesis of different crystallographic FeOOH catalysts for peroxymonosulfate activation towards organic matter degradation. *RSC Adv.* **2018**, *8*, 7269–7279. [[CrossRef](#)]
32. Yang, T.; Fan, S.; Li, Y.; Zhou, Q. Fe-N/C single-atom catalysts with high density of Fe-N_x sites toward peroxymonosulfate activation for high-efficient oxidation of bisphenol A: Electron-transfer mechanism. *Chem. Eng. J.* **2021**, *419*, 129590. [[CrossRef](#)]
33. Wang, H.; Guo, W.; Liu, B.; Wu, Q.; Luo, H.; Zhao, Q.; Si, Q.; Sseguya, F.; Ren, N. Edge-nitrogenated biochar for efficient peroxydisulfate activation: An electron transfer mechanism. *Water Res.* **2019**, *160*, 405–414. [[CrossRef](#)] [[PubMed](#)]
34. Xu, X.; Zhang, Y.; Zhou, S.; Huang, R.; Huang, S.; Kuang, H.; Zeng, X.; Zhao, S. Activation of persulfate by MnOOH: Degradation of organic compounds by nonradical mechanism. *Chemosphere* **2021**, *272*, 129629. [[CrossRef](#)] [[PubMed](#)]
35. Guo, T.; Jiang, L.; Wang, K.; Li, Y.; Huang, H.; Wu, X.; Zhang, G. Efficient persulfate activation by hematite nanocrystals for degradation of organic pollutants under visible light irradiation: Facet-dependent catalytic performance and degradation mechanism. *Appl. Catal. B Environ.* **2021**, *286*, 119883. [[CrossRef](#)]
36. Chen, X.; Duan, X.; Oh, W.-D.; Zhang, P.-H.; Guan, C.-T.; Zhu, Y.-A.; Lim, T.-T. Insights into nitrogen and boron-co-doped graphene toward high-performance peroxymonosulfate activation: Maneuverable N-B bonding configurations and oxidation pathways. *Appl. Catal. B Environ.* **2019**, *253*, 419–432. [[CrossRef](#)]
37. Cao, J.; Lai, L.; Lai, B.; Yao, G.; Chen, X.; Song, L. Degradation of tetracycline by peroxymonosulfate activated with zero-valent iron: Performance, intermediates, toxicity and mechanism. *Chem. Eng. J.* **2019**, *364*, 45–56. [[CrossRef](#)]
38. Du, X.; Zhang, Y.; Hussain, I.; Huang, S.; Huang, W. Insight into reactive oxygen species in persulfate activation with copper oxide: Activated persulfate and trace radicals. *Chem. Eng. J.* **2017**, *313*, 1023–1032. [[CrossRef](#)]
39. Lutze, H.V.; Kerlin, N.; Schmidt, T.C. Sulfate radical-based water treatment in presence of chloride: Formation of chlorate, inter-conversion of sulfate radicals into hydroxyl radicals and influence of bicarbonate. *Water Res.* **2015**, *72*, 349–360. [[CrossRef](#)]
40. Bennedsen, L.R.; Muff, J.; Søgaard, E.G. Influence of chloride and carbonates on the reactivity of activated persulfate. *Chemosphere* **2012**, *86*, 1092–1097. [[CrossRef](#)]
41. Ji, Y.; Dong, C.; Kong, D.; Lu, J. New insights into atrazine degradation by cobalt catalyzed peroxymonosulfate oxidation: Kinetics, reaction products and transformation mechanisms. *J. Hazard. Mater.* **2015**, *285*, 491–500. [[CrossRef](#)] [[PubMed](#)]
42. Qi, F.; Chu, W.; Xu, B. Modeling the heterogeneous peroxymonosulfate/Co-MCM41 process for the degradation of caffeine and the study of influence of cobalt sources. *Chem. Eng. J.* **2013**, *235*, 10–18. [[CrossRef](#)]
43. Zhang, T.; Zhu, H.; Croué, J.-P. Production of Sulfate Radical from Peroxymonosulfate Induced by a Magnetically Separable CuFe₂O₄ Spinel in Water: Efficiency, Stability, and Mechanism. *Environ. Sci. Technol.* **2013**, *47*, 2784–2791. [[CrossRef](#)] [[PubMed](#)]
44. Zhang, T.; Chen, Y.; Wang, Y.; Le Roux, J.; Yang, Y.; Croué, J.-P. Efficient Peroxydisulfate Activation Process Not Relying on Sulfate Radical Generation for Water Pollutant Degradation. *Environ. Sci. Technol.* **2014**, *48*, 5868–5875. [[CrossRef](#)] [[PubMed](#)]
45. Hayat, W.; Zhang, Y.; Hussain, I.; Huang, S.; Du, X. Comparison of radical and non-radical activated persulfate systems for the degradation of imidacloprid in water. *Ecotoxicol. Environ. Saf.* **2019**, *188*, 109891. [[CrossRef](#)]
46. Lee, H.; Kim, H.-I.; Weon, S.; Choi, W.; Hwang, Y.S.; Seo, J.; Lee, C.; Kim, J.-H. Activation of Persulfates by Graphitized Nanodiamonds for Removal of Organic Compounds. *Environ. Sci. Technol.* **2016**, *50*, 10134–10142. [[CrossRef](#)]
47. Chen, J.; Fang, C.; Xia, W.; Huang, T.; Huang, C.-H. Selective Transformation of β -Lactam Antibiotics by Peroxymonosulfate: Reaction Kinetics and Nonradical Mechanism. *Environ. Sci. Technol.* **2018**, *52*, 1461–1470. [[CrossRef](#)]
48. Yun, E.-T.; Lee, J.H.; Kim, J.; Park, H.-D.; Lee, J. Identifying the Nonradical Mechanism in the Peroxymonosulfate Activation Process: Singlet Oxygenation Versus Mediated Electron Transfer. *Environ. Sci. Technol.* **2018**, *52*, 7032–7042. [[CrossRef](#)]
49. Qin, J.; Dai, L.; Shi, P.; Fan, J.; Min, Y.; Xu, Q. Rational design of efficient metal-free catalysts for peroxymonosulfate activation: Selective degradation of organic contaminants via a dual nonradical reaction pathway. *J. Hazard. Mater.* **2020**, *398*, 122808. [[CrossRef](#)]
50. Yuan, R.; Jiang, M.; Gao, S.; Wang, Z.; Wang, H.; Boczkaj, G.; Liu, Z.; Ma, J.; Li, Z. 3D mesoporous α -Co(OH)₂ nanosheets electrodeposited on nickel foam: A new generation of macroscopic cobalt-based hybrid for peroxymonosulfate activation. *Chem. Eng. J.* **2019**, *380*, 122447. [[CrossRef](#)]
51. Huang, G.; Chuan-Wang, Y.; Yang, C.-W.; Guo, P.-C.; Yu, H.-Q. Degradation of Bisphenol A by Peroxymonosulfate Catalytically Activated with Mn_{1.8}Fe_{1.2}O₄ Nanospheres: Synergism between Mn and Fe. *Environ. Sci. Technol.* **2017**, *51*, 12611–12618. [[CrossRef](#)] [[PubMed](#)]
52. Huang, Z.; Ji, Z.-Y.; Zhao, Y.-Y.; Liu, J.; Li, F.; Yuan, J.-S. Treatment of wastewater containing 2-methoxyphenol by persulfate with thermal and alkali synergistic activation: Kinetics and mechanism. *Chem. Eng. J.* **2019**, *380*, 122411. [[CrossRef](#)]
53. Yang, S.; Wu, P.; Liu, J.; Chen, M.; Ahmed, Z.; Zhu, N. Efficient removal of bisphenol A by superoxide radical and singlet oxygen generated from peroxymonosulfate activated with Fe₀-montmorillonite. *Chem. Eng. J.* **2018**, *350*, 484–495. [[CrossRef](#)]
54. Feng, Y.; Lee, P.-H.; Wu, D.; Shih, K. Surface-bound sulfate radical-dominated degradation of 1,4-dioxane by alumina-supported palladium (Pd/Al₂O₃) catalyzed peroxymonosulfate. *Water Res.* **2017**, *120*, 12–21. [[CrossRef](#)]
55. Zhang, Q.; He, D.; Li, X.; Feng, W.; Lyu, C.; Zhang, Y. Mechanism and performance of singlet oxygen dominated peroxymonosulfate activation on CoOOH nanoparticles for 2,4-dichlorophenol degradation in water. *J. Hazard. Mater.* **2019**, *384*, 121350. [[CrossRef](#)]
56. Ding, D.; Yang, S.; Qian, X.; Chen, L.; Cai, T. Nitrogen-doping positively whilst sulfur-doping negatively affect the catalytic activity of biochar for the degradation of organic contaminant. *Appl. Catal. B Environ.* **2019**, *263*, 118348. [[CrossRef](#)]

57. Duan, X.; Sun, H.; Wang, Y.; Kang, J.; Wang, S. N-Doping-Induced Nonradical Reaction on Single-Walled Carbon Nanotubes for Catalytic Phenol Oxidation. *ACS Catal.* **2014**, *5*, 553–559. [[CrossRef](#)]
58. Zhu, S.; Huang, X.; Ma, F.; Wang, L.; Duan, X.; Wang, S. Catalytic Removal of Aqueous Contaminants on N-Doped Graphitic Biochars: Inherent Roles of Adsorption and Nonradical Mechanisms. *Environ. Sci. Technol.* **2018**, *52*, 8649–8658. [[CrossRef](#)]
59. Cheng, X.; Guo, H.; Zhang, Y.; Wu, X.; Liu, Y. Non-photochemical production of singlet oxygen via activation of persulfate by carbon nanotubes. *Water Res.* **2017**, *113*, 80–88. [[CrossRef](#)]
60. Zhu, S.; Li, X.; Kang, J.; Duan, X.; Wang, S. Persulfate Activation on Crystallographic Manganese Oxides: Mechanism of Singlet Oxygen Evolution for Nonradical Selective Degradation of Aqueous Contaminants. *Environ. Sci. Technol.* **2018**, *53*, 307–315. [[CrossRef](#)]
61. Li, H.; Tian, J.; Xiao, F.; Huang, R.; Gao, S.; Cui, F.; Wang, S.; Duan, X. Structure-dependent catalysis of cuprous oxides in peroxydisulfate activation via nonradical pathway with a high oxidation capacity. *J. Hazard. Mater.* **2019**, *385*, 121518. [[CrossRef](#)] [[PubMed](#)]
62. Guan, C.; Jiang, J.; Pang, S.; Luo, C.; Ma, J.; Zhou, Y.; Yang, Y. Oxidation Kinetics of Bromophenols by Nonradical Activation of Peroxydisulfate in the Presence of Carbon Nanotube and Formation of Brominated Polymeric Products. *Environ. Sci. Technol.* **2017**, *51*, 10718–10728. [[CrossRef](#)] [[PubMed](#)]
63. Norris, D.J.; Yao, N.; Charnock, F.T.; Kennedy, T.A. High-Quality Manganese-Doped ZnSe Nanocrystals. *Nano Lett.* **2000**, *1*, 3–7. [[CrossRef](#)]
64. Gorman, A.A.; Rodgers, M.A.J. Singlet molecular oxygen. *Chem. Soc. Rev.* **1981**, *10*, 205–231. [[CrossRef](#)]
65. Nardi, G.; Manet, I.; Monti, S.; Miranda, M.A.; Lhiaubet-Vallet, V. Scope and limitations of the TEMPO/EPR method for singlet oxygen detection: The misleading role of electron transfer. *Free Radic. Biol. Med.* **2014**, *77*, 64–70. [[CrossRef](#)] [[PubMed](#)]
66. Zhou, Y.; Jiang, J.; Gao, Y.; Ma, J.; Pang, S.-Y.; Li, J.; Lu, X.-T.; Yuan, L.-P. Activation of Peroxydisulfate by Benzoquinone: A Novel Nonradical Oxidation Process. *Environ. Sci. Technol.* **2015**, *49*, 12941–12950. [[CrossRef](#)]
67. Wang, M.; Cui, Y.; Cao, H.; Wei, P.; Chen, C.; Li, X.; Xu, J.; Sheng, G. Activating peroxydisulfate with Co₃O₄/NiCo₂O₄ double-shelled nanocages to selectively degrade bisphenol A—A nonradical oxidation process. *Appl. Catal. B Environ.* **2020**, *282*, 119585. [[CrossRef](#)]
68. Yao, C.; Zhang, Y.; Du, M.; Du, X.; Huang, S. Insights into the mechanism of non-radical activation of persulfate via activated carbon for the degradation of p-chloroaniline. *Chem. Eng. J.* **2019**, *362*, 262–268. [[CrossRef](#)]
69. Liang, C.; Huang, C.-F.; Mohanty, N.; Kurakalva, R.M. A rapid spectrophotometric determination of persulfate anion in ISCO. *Chemosphere* **2008**, *73*, 1540–1543. [[CrossRef](#)]